

UC Berkeley

UC Berkeley Previously Published Works

Title

Transferring orbital angular momentum to an electron beam reveals toroidal and chiral order

Permalink

<https://escholarship.org/uc/item/7sv8c4nr>

Journal

Physical Review B, 107(20)

ISSN

2469-9950

Authors

Nguyen, KX
Jiang, Y
Cao, MC
[et al.](#)

Publication Date

2023-05-01

DOI








10.1103/physrevb.107.205419

Copyright Information

This work is made available under the terms of a Creative Commons Attribution-NonCommercial-ShareAlike License, available at <https://creativecommons.org/licenses/by-nc-sa/4.0/>

Peer reviewed

Transferring orbital angular momentum to an electron beam reveals toroidal and chiral order

K. X. Nguyen ^{1,2,*}, Y. Jiang,³ M. C. Cao ², P. Purohit ³, A. K. Yadav,⁴ P. García-Fernández,⁵ M. W. Tate,³ C. S. Chang ³, P. Aguado-Puente,^{6,7} J. Íñiguez,^{8,9} F. Gomez-Ortiz ⁵, S. M. Gruner ^{3,10,11}, J. Junquera,⁵ L. W. Martin,^{12,13} R. Ramesh,^{12,14} and D. A. Muller ^{2,10,†}

¹*Department of Chemistry and Chemical Biology, Cornell University, Ithaca 14853, New York, USA*

²*School of Applied and Engineering Physics, Cornell University, Ithaca 14853, New York, USA*

³*Department of Physics, Cornell University, Ithaca 14853, New York, USA*

⁴*Department of Electrical Engineering and Computer Sciences, University of California, Berkeley 94720, California, USA*

⁵*Departamento de Ciencias de la Tierra y Física de la Materia Condensada, Universidad de Cantabria, Cantabria Campus Internacional, Avenida de los Castros s/n, 39005 Santander, Cantabria, Spain*

⁶*Atomistic Simulation Center, Queen's University Belfast, Belfast BT7 1NN, Northern Ireland, United Kingdom*

⁷*CIC nanoGUNE BRTA, E-20018 Donostia-San Sebastian, Spain*

⁸*Materials Research and Technology Department, Luxembourg Institute of Science and Technology (LIST), 5 avenue des Hauts-Fourneaux, Esch-Sur-Alzette L-4362, Luxembourg*

⁹*Physics and Materials Science Research Unit, University of Luxembourg, 41 Rue du Brill, Belvaux L-4422, Luxembourg*

¹⁰*Kavli Institute at Cornell for Nanoscale Science, Ithaca 14853, New York, USA*

¹¹*Cornell High Energy Synchrotron Source (CHESS), Cornell University, Ithaca 14853, New York, USA*

¹²*Department of Material Science and Engineering, University of California, Berkeley, Berkeley 94720, California, USA*

¹³*Materials Sciences Division, Lawrence Berkeley National Laboratory, Berkeley 94720, California, USA*

¹⁴*Department of Physics, University of California, Berkeley 94720, California, USA*



(Received 6 February 2023; revised 30 April 2023; accepted 2 May 2023; published 26 May 2023)

Orbital angular momentum (OAM) and torque transfer play central roles in a wide range of magnetic textures and devices including skyrmions and spin-torque electronics. Analogous topological structures are now also being explored in ferroelectrics, including polarization vortex arrays in ferroelectric/dielectric superlattices. Unlike magnetic toroidal order, electric toroidal order does not couple directly to linear external fields. Instead, we find that the presence of an electric toroidal moment in a ferrorotational phase transfers measurable torque and OAM to a localized electron beam in the ballistic limit. We record these torque transfers from a high-energy electron beam using a momentum-resolved detector. This approach provides a high-sensitivity method to detect polarization fields and their more complex order parameters and topologies. In addition to toroidal order, we also demonstrate high-precision measurements of vorticity and chirality for polar vortexlike phases.

DOI: [10.1103/PhysRevB.107.205419](https://doi.org/10.1103/PhysRevB.107.205419)

I. INTRODUCTION

Topological states of electrical polarization have emerged as an area of research having both fundamental [1,2] and technological relevance [3]. While absent in bulk, nontrivial polarization field textures, including structures with ferroaxial or toroidal order parameters, were predicted to arise from the close interplay between the geometry of low-dimensional structures and the topology of the polarization field $\mathbf{P}(\mathbf{r})$ [4,5], where \mathbf{r} locates the position of the local polarization. The resulting vortexlike topological features which arise from continuous rotations of the polarization field can be characterized by the electric toroidal moment order parameter $\mathbf{g} = \frac{1}{2} \int \mathbf{r} \times \mathbf{P}(\mathbf{r}) d^3\mathbf{r}$ [6–8], giving rise to a host of coupling mechanisms (e.g., pyrotoroidic, piezotoroidic, electric

toroidal susceptibility). Theoretical studies have suggested possible routes to control ferroelectric toroidal order parameters in ferroelectric nanostructures [9–13], and recently, ordered vortexlike textures of electrical polarization have been experimentally stabilized [2]. These were achieved in $(\text{SrTiO}_3)_x/(\text{PbTiO}_3)_x$ superlattices [2], where the balance between electrostatic and strain boundary conditions resulted in nanometer-scale polarization vortex arrays possessing an electric toroidal moment. In addition, variant topological domains have been observed in ferroelectric perovskite thin films such as flux closures [14], skyrmions [15], and merons [16]. While the discovery of these emerging topological ferroelectrics has been promising for future technologies such as spin-torque electronics [17–20], understanding the underlying physical phenomena within these structures can reveal mechanisms to control and switch them in real devices. One example is utilizing soft x-ray dichroism measured on polarization vortices to investigate the underlying macroscopic chirality from ordered regions of vortexlike polar line defects [21]. While

*kn324@cornell.edu

†david.a.muller@cornell.edu

these studies provide a spatially averaged measurement of the ferrotoroidal state, the microscopic details of the chiral nature of this phase are still unclear.

Here, we show how the toroidal moment can be directly measured, with high sensitivity and spatial resolution, using (i) a generation of momentum-resolved electron microscope pixel array detectors (EMPADs) and (ii) the proportional relationship between the orbital angular momentum (OAM) transferred to the electron beam \mathbf{L} and the toroidal moment of the superlattice \mathbf{g} . Our technique can recover torque transfer and OAM with high fidelity and resolution, without compromising the beam shape, and in a geometry where it is possible to simultaneously measure and distinguish electric fields, polarity, and crystal tilt, the latter being a serious challenge for traditional approaches such as holography and differential phase contrast [22]. Furthermore, our approach is based on spatially resolved diffraction that has already demonstrated subpicometer precision for nonpolar measurements [23], as it is insensitive to the scan instabilities that limit conventional approaches to 5–10 pm uncertainty. This increased sensitivity is needed to allow us to take differential measures of the polarity fields such as the vorticity $\nabla \times \mathbf{P}(\mathbf{r})$. The underlying center-of-mass (COM) analysis for mapping polarity described in our arXiv preprint [24] of this paper has already proved useful for observing chirality and resolving handedness in vortexlike phases [25].

II. EXPERIMENTAL AND THEORETICAL METHODS

Superlattice samples were imaged using an in-focus probe with a semiconvergence angle of 3 mrad at 200 keV (depth of focus ~ 280 nm) on an uncorrected FEI Tecnai F20. For our 60–300 keV FEI Titan Themis experiments, we also imaged using an in-focus probe as well and a 1.72 mrad semiconvergence angle at 300 keV (depth of focus ~ 666 nm). Typical beam currents and dwell times were ~ 20 pA and 1 ms. The same EMPAD was used on both instruments. Pulsed laser deposition was used to synthesize superlattice films of $\text{PbTiO}_3/\text{SrTiO}_3$. All films were grown on SrRuO_3 -buffered (110)-oriented DyScO_3 single-crystalline substrate. Reflection high-energy electron diffraction was used to monitor the growth dynamics of PbTiO_3 and SrTiO_3 . The growth conditions were carefully optimized to obtain layer-by-layer (Frank–van der Merwe) growth of PbTiO_3 and SrTiO_3 , which was sustained for the entire growth of 100-nm-thick superlattice film. For a detailed account on growth conditions and optimization of other parameters, see the Methods sections of Refs. [2,26].

Atomic simulations of the $\text{PbTiO}_3/\text{SrTiO}_3$ superlattice use potentials that are identical to those in Ref. [27]. The interactions within the PbTiO_3 or SrTiO_3 layers were based on the previously introduced potentials for the bulk compounds, which give a qualitatively correct description of the lattice dynamical properties and structural phase transitions of both materials. For the interactions between ion pairs at the interface, simple numerical averages were used. For the periodicities of the superlattices studied in this paper, the main effects of the stacking are purely electrostatic. Those long-range dipole-dipole interactions are governed by the Born effective charges of the bulk parent compounds

and a bare electronic dielectric constant ϵ^∞ that is taken as a weighted average of the first-principles results for bulk PbTiO_3 ($\epsilon^{\infty,\text{PTO}} = 8.5$) and SrTiO_3 ($\epsilon^{\infty,\text{STO}} = 6.2$) with weights reflecting the composition of the superlattice. To preserve the electrostatic interactions within each material as close as possible to the bulk parent compounds, we have rescaled the Born effective charge tensors of the inner atoms by $\sqrt{\epsilon^\infty/\epsilon^{\infty,\text{ABO}_3}}$ (where ABO_3 stands for PbTiO_3 or SrTiO_3 depending on the layer to which the atom belongs). In this way, following eq. (23) of Ref. [28], the dipole-dipole interactions remain the same as in bulk even if we adopt a common value of ϵ^∞ for the whole heterostructure. The Born tensors corresponding to the atoms at the interfaces were left untouched.

We assume in-plane lattice constants of $a = b = 3.901$ Å and $\gamma = 90^\circ$. To counteract the underestimate of the lattice constant due to the well-known overbinding error of the local density approximation, which is the first-principles theory used to compute the parameters of our model, an external expansive hydrostatic pressure of -11.2 GPa is imposed. These approximations and adjustments allow us to construct models for superlattices of arbitrary n stacking. For computational feasibility, we have focused on a simulation supercell made from a periodic repetition of $2n \times n \times 2n$ elemental perovskite unit cells, sufficiently large to simulate domains in the $n = 10$ superlattice. We solved the models by running Monte Carlo simulations typically comprising 10 000 thermalization sweeps followed by 40 000 sweeps to compute thermal averages. We ran Monte Carlo simulated annealing down to very low temperatures to perform structural relaxations and found the ground state or metastable solutions.

III. RESULTS

To date, the electron microscopy approach to measuring OAM has been to start with a beam that has been structured with special apertures to possess a well-defined OAM, such as a vortex beam. In this approach, the vortex beam scatters through the sample, and a change is recorded with a localized detector. This approach has been used for magnetic measurements from inelastic scattering [29–32] but precludes the simultaneous momentum measurements needed to reliably recover polarity in ferroelectrics. Our approach is, in a sense, to run this experiment backwards, i.e., using a simple and local beam (i.e., with zero OAM), and having it scatter through a sample that has vorticity where the final OAM is recorded with an angle-resolved and phase-sensitive detection method. There are also schemes to build OAM eigenvalue sorters where the detector is also placed after the sample, and while promising, they currently lack the spatial resolution or sensitivity needed for polarization detection [33,34]. Our approach is enabled by a four-dimensional scanning transmission electron microscopy (4D-STEM) with the EMPAD [35], schematized for the case of a $(\text{PbTiO}_3)_{12}/(\text{SrTiO}_3)_{12}$ superlattice in Fig. 1(a). In this way, we can simultaneously measure the linear momentum transfer to the scattered electron beam $\langle \mathbf{p} \rangle$, which recovers polarity [26,36] by measuring the probability current flow [35,37,38] in ferroelectric polar vortices, and develop an approach to measure OAM, detailed in the following section.

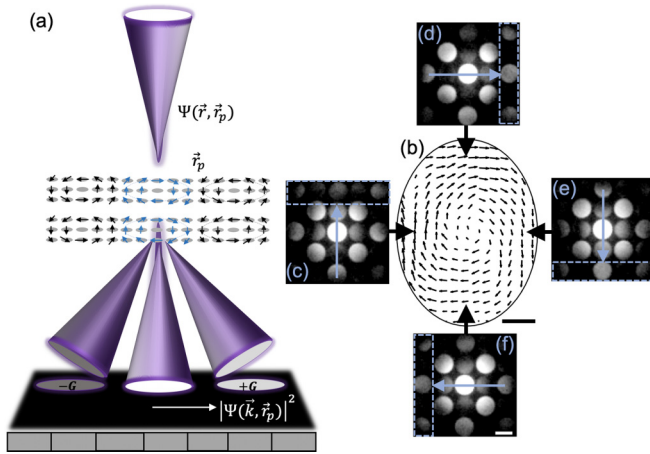


FIG. 1. Measuring complex polarization textures with electron microscopy pixel array detector (EMPAD). (a) Schematic of EMPAD placed in the diffraction plane, where a convergent beam electron diffraction (CBED) pattern is formed at the detector. Polarity causes an asymmetry in intensities of the conjugated pairs of diffracted disks at $+G$ and $-G$, where G is the reciprocal lattice vector, indicated as light and dark gray disks. We utilize this aspect of the electron scattering distribution by taking the probability current flow to track the change in polarization around a single vortex. (b) A single vortex shown with corresponding CBED patterns observed in different regions of the vortex (c)–(f) show how the CBED patterns change with respect to position. Scale bar in (b) is 1 nm and in (f) is 6 mrad for the CBED patterns in (c)–(f).

Using this approach, we can see the change in polarization around each vortex directly in our convergent beam electron diffraction (CBED) patterns (Fig. 1) and find that the intensity of the CBED patterns observed in different regions of the vortex [Figs. 1(c)–1(f)] changes direction with the polarization. The polarization texture [Fig. 1(b)], where the local dipoles within the PbTiO_3 layer continuously rotate forming a sequence of clockwise/counterclockwise arrays of vortices along the $[100]$ direction, obtained with this method is perfectly compatible with the one observed by high-resolution transmission electron microscopy [2] but has a much higher signal-to-noise (SNR) ratio and can now resolve details of the decay of the fringe field into the SrTiO_3 layer.

Utilizing information from 4D-STEM, we use ptychography [39–41] to first calculate OAM of the probe by explicitly calculating

$$\langle \mathbf{L} \rangle = \langle \Psi | \hat{\mathbf{r}} \times \hat{\mathbf{p}} | \Psi \rangle = \int \Psi^*(\mathbf{r}) [\hat{\mathbf{r}} \times \hat{\mathbf{p}}] \Psi(\mathbf{r}) d\mathbf{r}, \quad (1)$$

where Ψ is the exit wave function of the electron beam after scattering in the sample, \mathbf{r} is the probe coordinate in real space with respect to the incident probe position, and $\hat{\mathbf{r}}$ and $\hat{\mathbf{p}}$ are the position and momentum operators, respectively. Experimentally, within nonoverlapping diffraction disks, there is a finite width to their size and an intrinsic uncertainty such that a relation between $\hat{\mathbf{r}}$ and $\hat{\mathbf{p}}$ becomes measurable. Furthermore, we find that this method recovers the phase and amplitude of the exit wave function and is exact for all sample thicknesses to within the accuracy of the ptychographic reconstruction.

However, ptychography is computationally intensive and requires high sampling densities in real space.

Here, we also propose a faster and more efficient two-step approach that is less restricted by in-plane sampling requirements. The first step is a change in the focus from the direct measurement of the OAM to the change (derivative) of its expectation value. This is given by the torque exercised by the sample on the probe $\langle \mathbf{\Gamma} \rangle$, given by

$$\langle \mathbf{\Gamma} \rangle = \frac{d\langle \mathbf{L} \rangle}{dt} = \langle \Psi | [\mathbf{r} \times (-\nabla V)] | \Psi \rangle, \quad (2)$$

where V is the sample potential [see Appendix B, Eq. (B4)] [42].

The second step is to take the integral over time of $\langle \mathbf{\Gamma} \rangle$ in Eq. (2) to get the total change of the expectation value of $\langle \mathbf{L} \rangle$. For elastic scattering, the electron travels at constant velocity where the integration over time for the propagation of the wave packet through the sample becomes an integration over sample thickness. We then use the strong phase approximation to connect the probability current images (\mathbf{p}) [Fig. 2(d)] to ∇V [Appendix B, Eqs. (B8)–(B18)] [43–47]. The result provides the z component of the torque (in the coordinate system of the microscope) convolved incoherently with the probe shape, where the electron trajectory as a diffraction-limited electron probe with incident wave packet $\Psi_0(\vec{r} - \vec{r}_p)$ centered about incident probe position \vec{r}_p :

$$\langle \Gamma_z(\mathbf{r}_p) \rangle = \int \{(\vec{r} - \vec{r}_p) \times [-\nabla V(\vec{r})]\}_z |\Psi_0(\vec{r} - \vec{r}_p)|^2 d\vec{r}, \quad (3)$$

which can be separated in Fourier space, and then corrected for probe shape [Eq. (B18)]. Since we are imaging in projection, the passage of the beam through the sample gives $\langle L_z \rangle = \int \langle \Gamma_z \rangle dt$. Here, we need to integrate this expectation value over the thickness of the specimen, giving us noninteger values of OAM.

To test the numerical accuracy of both ptychographic and torque transfer approaches, we perform the multislice simulations [42] on the model polarization vortex structures. Figure 2(e) shows the change in OAM calculated using ptychography, and Fig. 2(f) is the total torque transfer $\langle L_z \rangle$, calculated from $\langle p_x \rangle$ and $\langle p_y \rangle$ images using Eq. (B18); here, we find that there is good agreement between the angular momentum and torque transfer approaches for a moderate thickness sample (< 20 nm). In thick simulated samples, the two approaches begin to diverge as the strong phase approximation breaks down once beam propagation effects become significant (Fig. 3).

We then utilize our faster, efficient torque transfer approach on experimental results of the $(\text{PbTiO}_3)_{12}/(\text{SrTiO}_3)_{12}$ superlattice. First, we plotted the $\{200\}$ probability current in Fig. 4(a) as a vector map to show the ordered arrays of polarization vortices, where we find the vortices have offset cores and slightly asymmetric shapes. Second, we show the measured $\langle L_z \rangle$ [Fig. 4(b)] using the total torque transfer [Eq. (B18)] from the same region as Fig. 4(a) at high and low magnification in Fig. 4(d), where we make picometer-precision measurements over arbitrarily large fields of view. We find that our detection scheme overcomes a limitation of real-space imaging; here, the sensitivity is set by the SNR on the detector in momentum space, rather than the

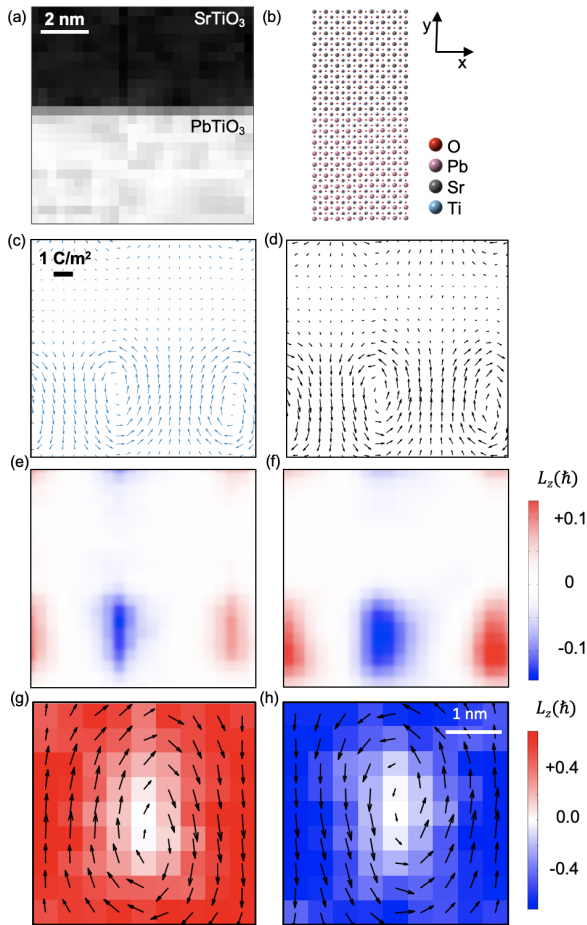


FIG. 2. Cross-sections along the vortex axis for a simulated 10×10 $\text{PbTiO}_3/\text{SrTiO}_3$ superlattice: (a) ADF image from reconstruction and (b) atomic-model structure of the superlattice. (c) “2nd principles” calculation of the polarization field. (d) Reconstructed vortices from $\langle p_x \rangle$ and $\langle p_y \rangle$ images of the (200) and $(\bar{2}00)$ diffracted disks calculated from the propagation of the electron beam through the simulated structure. (e) Change in orbital angular momentum reconstructed from the full wave function and (f) integrated torque transfer from the electron to the sample calculated from Eq. (B18) showing good agreement with the exact momentum transfer. Calculated vortex $L_z = \langle \mathbf{r} \rangle \times \langle \mathbf{p} \rangle$ with coordinates centered at center of a vortex from reconstructed vortices from $\langle p_x \rangle$ and $\langle p_y \rangle$ images of the diffracted disks showing (g) clockwise and (h) counter-clockwise rotations.

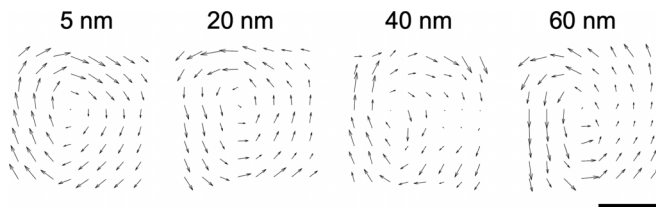


FIG. 3. Reconstructed vortices from $\langle p_x \rangle$ and $\langle p_y \rangle$ images of the (200) and $(\bar{2}00)$ diffracted disks calculated from a simulated structure at thicknesses of 5, 20, 40 and 50 nanometers. Here, we observed that channeling of the electron beam causes the polarization direction to switch depending on the thickness with a period of 20 nanometers, reflecting contrast reversals in the underlying $\{200\}$ diffraction peaks from dynamical scattering in the sample. Black scale bar represents 3 nanometers.

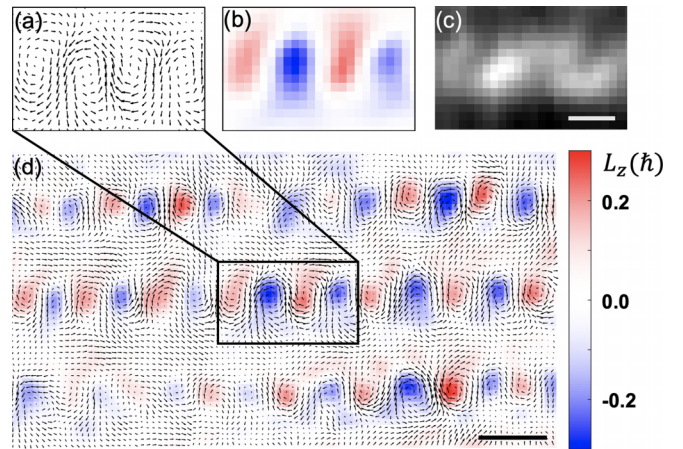


FIG. 4. Using our analysis of polarity and analytical expression for orbital angular momentum (OAM), we can use our results to extract the OAM of the polarization vortices quantitatively. (a) Polarity vortices reconstructed from experimentally measured $\langle p_x \rangle$ and $\langle p_y \rangle$ along with (b) the measured torque transfer to electron beam for the same region and (c) ADF image of the region. (d) Larger field of view of the sample showing torque transfer overlaid with the polarity map. Colorbar shows the change in angular momentum from the torque transfer in units of \hbar . Black scale bar in (b) is 2 nanometers and (c) is 5 nanometers.

picometer-scale instabilities in the scan position of the electron beam, since it is no longer necessary to resolve and count individual atoms. Furthermore, our approach measures both linear and angular momentum, where beam $\langle \mathbf{L} \rangle$ measures the vorticity and the sample $\langle \mathbf{L} \rangle$ takes on an additional significance, as it is proportional to the toroidal moment and order parameter \mathbf{g} (see Appendix B) for ferroaxial textures.

For reasonably thin specimens where the strong phase approximation holds [Eq. (B7)], the probability current images can be further simplified as a convolution of the incident beam shape and the gradient of the sample potential $V(\vec{r}_p)$ [47]:

$$\langle \vec{p}(\vec{r}_p) \rangle = \hbar \sigma |\Psi_0(\vec{r}_p)|^2 \otimes \vec{\nabla} V(\vec{r}_p), \quad (4)$$

from which we can now calculate and measure the OAM $\langle \mathbf{L} \rangle$. We note that $\langle \mathbf{L} \rangle (= \hat{\mathbf{r}} \times \hat{\mathbf{p}})$ is proportional to the toroidal moment and order parameter $\mathbf{g} = \frac{1}{2} \int \mathbf{r} \times \mathbf{P}(\mathbf{r}) d^3 \mathbf{r}$, where $\mathbf{P}(\mathbf{r})$ is local dipole density [6], as $\mathbf{P}(\mathbf{r})$ is proportional to $\langle \mathbf{p} \rangle$ constructed from Friedel pairs in thin samples. This can be seen numerically in Fig. 2(c) vs Fig. 2(d), where the polarization field tracks the contrast in the probability current images $\langle p_x \rangle$ and $\langle p_y \rangle$.

There are two different orbital angular momenta that we can measure: that of the beam and the sample. When the beam is much smaller than the sample, the OAM of the beam maps the local vorticity, i.e., the beam is rotated by the curl of the vector field, in this case, $\nabla \times \vec{P}$. In this way, the angular momentum that we are measuring comes from a torque that is applied perpendicular to the direction of the motion of the electron beam causing a change to the OAM of the electron beam and not its spin angular momentum [48]. This is like putting a small float into a vortex and watching its rotation. It will be maximal at the center of the vortex. Furthermore, a nonzero $\nabla \times \vec{P}$ is a very important signature for distinguishing

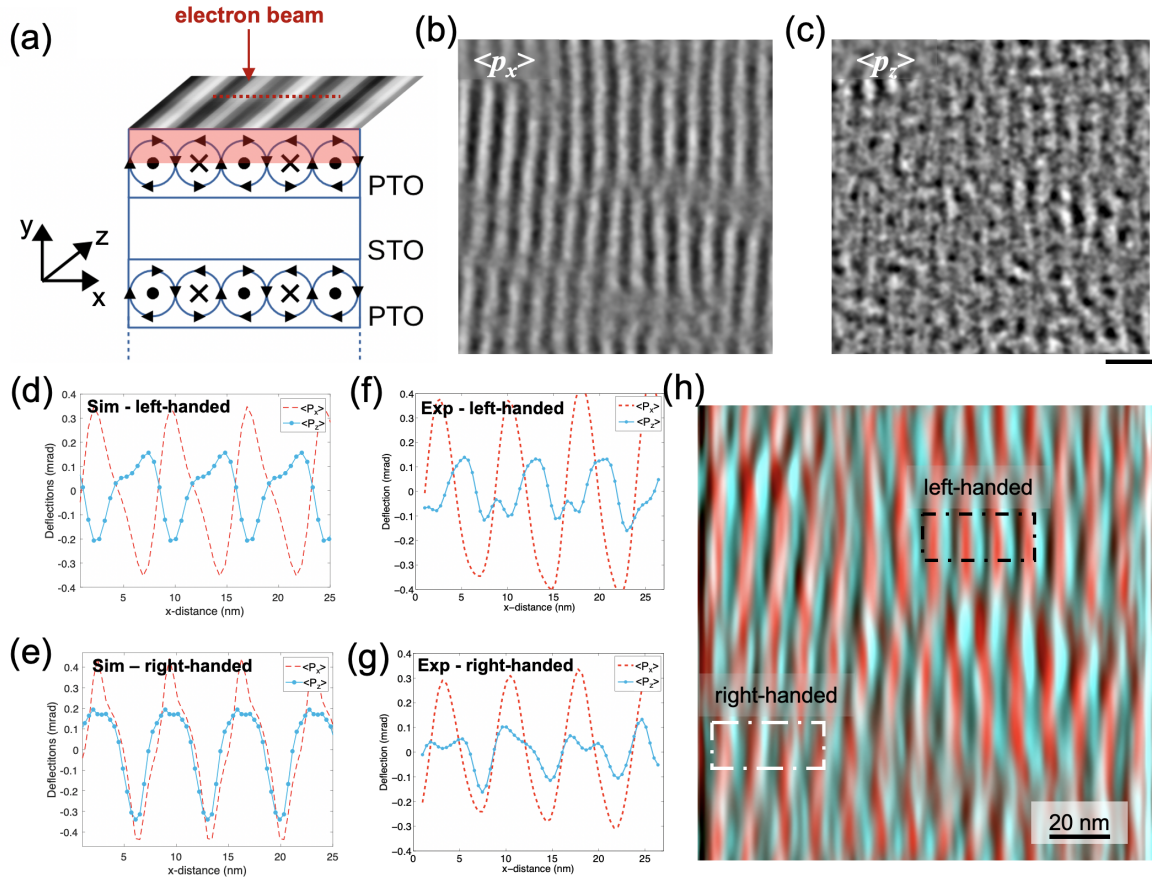


FIG. 5. Plane view imaging of the polarization textures. The underlying polarization texture relative to the electron microscope image is sketched in (a), where vortices in the superlattice are represented as arrows describing circles in the (x, y) plane plus dots and crosses indicating polarization pointing along the positive or negative z axis. Here, the top half of the vortices is highlighted in red representing the fact that the probability current signal comes mostly from the top half of the vortices [see text and Figs. 6(c)–6(d)]. Experimental images of (b) $\langle p_x \rangle$ and (c) $\langle p_z \rangle$ images from a 12×12 superlattice using a 1.4 mrad semiconverged angle probe at 300 keV. We observed that the stripes have higher contrast in $\langle p_x \rangle$ than in $\langle p_z \rangle$, although faint contrast is seen in $\langle p_z \rangle$. Full multiple scattering simulations of electron beam propagation through structures calculated by “2nd principles” calculation of the polarization field for a 10×10 superlattice show projected polarization of $\langle p_x \rangle$ and $\langle p_z \rangle$ as line profiles for both (d) right-handed and the (e) left-handed chiral structures and are in good agreement with experiment. Experimentally, we overlay our results from (b) $\langle p_x \rangle$ and (c) $\langle p_z \rangle$ images with false color in (h), red and cyan respectively. From the line profiles in (h) at two different regions in the same image, we observed both (f) right-handed and (g) left-handed chirality in different domain regions. Black scale bar under (c) represents 20 nm.

a vortex phase from the classical Kittel flux-closure domain [49]. The OAM of the vortex itself can also be calculated from $L_z = \langle \vec{r} \times \langle \vec{p} \rangle \rangle$ where r is now the coordinate centered on the vortex and not the beam, as shown in Figs. 2(g) and 2(h). As expected, the OAM at the center of the vortex goes to zero. Consequently, we find that we can utilize this approach to uncover the theoretically predicted [27] chiral nature of the vortex states. Here, Fig. 4(d) shows the toroidal ordering is that of off-centered, alternating, and asymmetric vortices that lack an axis of symmetry. This is a necessary but not sufficient condition for chirality.

To determine if the vortex structures are chiral in three dimensions, we need to also investigate if there is net polarization along the axial direction of the vortex. To do this, we prepared plan-view thinned samples of the $(\text{PbTiO}_3)_{12}/(\text{SrTiO}_3)_{12}$ superlattice and imaged down the [001] zone of the superlattice [Fig. 5(a)]. In this orientation, the net polarity needed for a chiral structure will appear as a nonzero $\langle p_z \rangle$ component on the EMPAD (again, x and y

are in the detector coordinate system with z along the axial direction of the vortices). Figures 5(b) and 5(c) show $\langle p_x \rangle$ and $\langle p_z \rangle$ images, respectively, where a small but nonzero $\langle p_z \rangle$ is indeed detected, having 6 times less intensity than $\langle p_x \rangle$ (Fig. 6). The reduced axial intensity is a consequence of the strong dechanneling of the electron beam on lead atom columns (Fig. 7), which means we do not sample all depths through the sample with equal weighting; here, we observed that most of our signal for $\langle p_x \rangle$ and $\langle p_z \rangle$ comes from the top half of the vortices [shown as the red-shaded region in Fig. 5(a)]. This reduces sensitivity to the axial component and is present both for our method and the less-sensitive high-angle annular dark-field (ADF)-based method to measure polar displacements. By comparing second-principles simulations of the projected polarization for left- and right-handed chiral structures [Figs. 5(d) and 5(e)], we again see the polarization weighted from beam propagation toward the entrance surface. Here, we observed that a left-handed chiral structure shows $\langle p_x \rangle$ and $\langle p_z \rangle$ components out of phase,

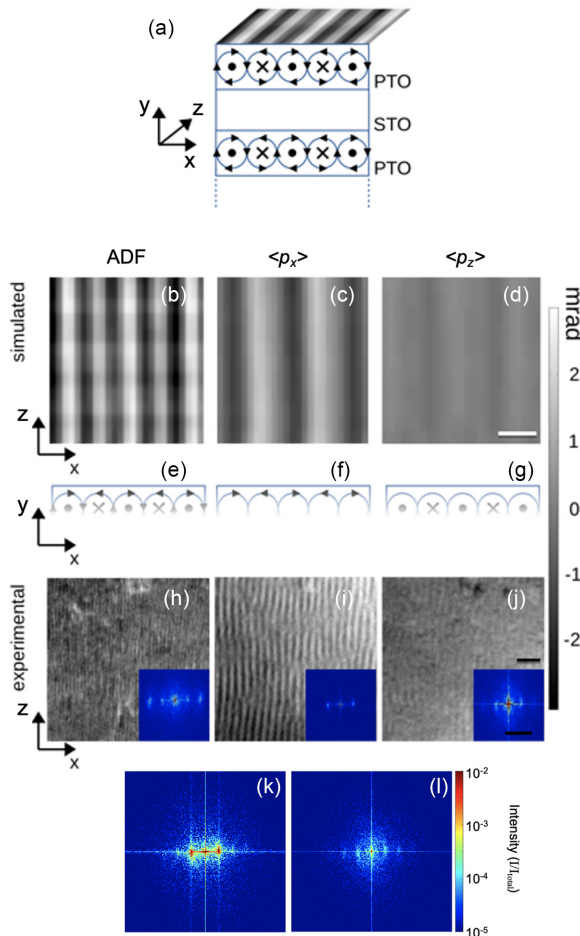


FIG. 6. Plane view imaging of the polarization textures. The underlying polarization texture relative to the electron microscope image is sketched (a), where vortices in the superlattice are represented as arrows describing circles in the (x, y) plane plus dots and crosses indicating polarization pointing along the positive or negative y axis. (b) Annular dark field (ADF), (c) $\langle p_x \rangle$ and (d) $\langle p_z \rangle$ images reconstructed from the coordinates of a 10×10 superlattice using 1.76 mrad semiconverged angle probe at 300 keV. (e)–(g) Show the features of the polarization texture for which the measurements in the panels above and below are sensitive. The fading of the sketches in (e)–(g) represent the fact that the probability current signal comes mostly from the top half of the vortices (see text). Experimental results from 12×12 superlattice using the same imaging parameters as simulation for (h) ADF, (i) $\langle p_x \rangle$ and (j) $\langle p_z \rangle$. By looking at a larger field of view in (h) ADF, and probability current flow (i) $\langle p_x \rangle$ and (j) $\langle p_z \rangle$ we observed that the stripes have higher contrast in $\langle p_x \rangle$ than in $\langle p_z \rangle$, although faint contrast is seen in $\langle p_z \rangle$. Fourier transforms (FT) of (h)–(j) is represented as insets to each figure respectively. Here, we observed double periodicity in the FT (j) of the ADF. For (i) $\langle p_x \rangle$ and (j) $\langle p_z \rangle$, we added the ratio of their intensities to the total intensity of their FTs to show single periodicity with the (k) FT of $\langle p_x \rangle$ having 6 times more intensity than the (l) FT of $\langle p_z \rangle$. White scale bar in (d) represents 5 nm. Black scale bar under (j) represents 30 nm.

whereas a right-handed chiral structure has them tracking one another. Experimental results for $\langle p_x \rangle$ and $\langle p_z \rangle$ [Figs. 5(b) and 5(c)] are superimposed to visualize their relative alignments in Fig. 5(h). We observed both left- and right-handed chiral

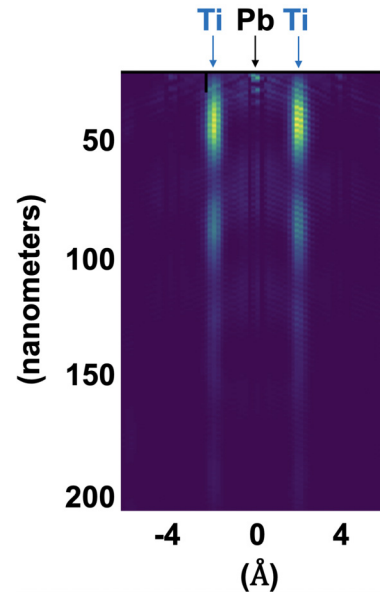


FIG. 7. Multislice simulation of 6×6 $\text{PbTiO}_3/\text{SrTiO}_3$ down the $[001]$ zone axis using 1.76-mrad convergence angle at 300 keV. Multislice conditions are the same as experimental conditions used to those recorded with the electron microscopy pixel array detector (EMPAD) on a FEI Titan Themis.

domains [Figs. 5(f) and 5(g), respectively]; the small domain size (50–100 nm) could account for the weak chiral signal observed by x-ray scattering [21], where the superposition of both domains would reduce the net macroscopic chiral signal. In contrast, from both our simulation and experiment, we find that this should be a strongly chiral material within each domain but overall exhibiting both right- and left-handed chiral domains in proximity.

Electron channeling plays an important role in the depth dependence of the probability current signal where the signal is not a simple projection through the sample. The dechanneling in the two in-plane directions is quite similar, as it is dominated by the atomic column more so than the small displacements, where so much of the thickness variation can be compensated by comparing the relative intensities of the $\langle p_x \rangle$ and $\langle p_z \rangle$ components (Fig. 5). Although, electron channeling plays an important role in the depth dependence of the probability current signal where the signal is not a simple projection through the sample, we find that vorticity of the reconstructed vortices is retained at thicknesses of 5, 20, 40, and 50 nm in Fig. 3. Furthermore, we observed that electron dechanneling causes the polarization direction to switch depending on the thickness with a period of 20 nm, reflecting contrast reversals in the underlying $\{200\}$ diffraction peaks from dynamical scattering in the sample. By matching the measured diffraction patterns to the multislice simulations, we found the thickness of the plan-view transmission electron microscopy sample to be 21 ± 2 nm.

When looking at the structure of the polarization vortices along the axial direction, we imaged down the $[001]$ (plan view). Electron channeling causes most of the signal to be generated toward the entrance surface of the beam and thus weights information toward the upper half of the vortex, with

far less from the bottom half of the vortex structure. To interpret the contrast that we expect for $\langle p_x \rangle$ and $\langle p_z \rangle$, we use multislice simulations [Figs. 6(c) and 6(d)], which are in good agreement with the experimental results [Figs. 6(i) and 6(j)]. Relating this result to effects of the electron beam channeling down [001] in Fig. 7 and extended data fig. 7(d) of Ref. [15], we find that the probe wave function peaks and scatters early in the sample where $\langle p_x \rangle$ is larger, and $\langle p_z \rangle$ is still small. This asymmetric weighting is present in both diffraction and ADF measurements and can be tuned by changing the convergence angle. We note that, if the channeling were not present, the $\langle p_x \rangle$ signal in the upper half of the vortex would cancel that in the lower half and become unmeasurable in projection.

IV. SUMMARY

By applying our detection methods for mapping polar and toroidal order, we directly observe the emergence of chirality in such vortices. Furthermore, our approach to investigate these more complex polar orders at the length scale of a single vortex can be used for future investigations of possible chiral nature in other topological ferroelectric materials, e.g., Refs. [14–16]. The approach is especially valuable for multilayer heterostructures, which are often too thick for reliable direct imaging by ADF STEM, as the ADF signal is generated too close to the entrance surface (<6 nm) to measure the buried ferroelectric layer. As shown here, the more parallel beam used for the diffraction-based approach provides a directly interpretable signal up to ~ 20 nm, and the signal is still strong and readily quantified in thicker samples once corrections for sample thickness are made—this can help to minimize the effect of surface relaxation on the polar order. Sample thickness can be determined locally by matching to diffraction simulations. Our direct experimental approach shows that one can take two materials that by themselves are nonhanded but, when assembled under certain boundary conditions in which the two primary energy scales (the elastic and electrostatic energies), are almost of the same order of magnitude, and they compete with one another. This leads to order parameter topologies that are chiral with a characteristic length scale of 5–10 nm. Finally, we note that, although the calculations of torque transfer were performed for high-energy electrons, the same symmetry elements and invariants are also present in Bloch wave theory [50], suggesting that a similar scattering mechanism may be detectable in the ballistic limit with low-energy (i.e., few electronvolts) electrons as well, giving an electrical read-out mechanism for toroidal order that would be useful for interrogating a ferroelectric equivalent of a magnetic racetrack memory.

All data needed to evaluate the conclusions are present in this paper. Additional data related to this paper may be requested from the authors.

ACKNOWLEDGMENTS

Y.J., D.A.M., and ptychography supported by the U.S. Department of Energy, Grant No. DE-SC0002334. Electron microscopy experiments by K.X.N. and equipment supported by the Cornell Center for Materials Research, through the National Science Foundation MRSEC program, Award No. DMR-1719875. Torque transfer theory (M.C.) supported by

the Air Force Office of Scientific Research through the 2D Electronics MURI Grant No. FA9550-16-1-0031. Support for the MM-PAD development in S.M.G.'s lab was provided by the U.S. Department of Energy, Grant No. DE-FG02-10ER46693. The adaptation to the STEM was supported by the Kavli Institute at Cornell for Nanoscale Science. J.I. acknowledges support from the Luxembourg National Research Fund under Grant No. C15/MS/10458889 NEWALLS. P.G.F. and J.J. acknowledge financial support from the Spanish Ministry of Science, Innovation and Universities through Grant No. PGC2018-096955-B. R.R. acknowledges support from the Quantum Materials program funded by the U.S. Department of Energy, Office of Science. The authors acknowledge discussions with Robert Hovden, Lena Fitting-Kourkoutis, and Megan E. Holtz and microscopy facility support from John Grazul and Mariena Silvestry Ramos.

K.X.N. and D.A.M. designed the project. Electron microscopy and data analysis were carried out by K.X.N. and D.A.M.; PTO/STO superlattice samples grown by A.K.Y. under supervision of R.R. Electron microscope image simulation by Y.J., K.X.N., and M.C. Ptychography simulations were done by Y.J., supervised by D.A.M. Second-principles simulations were carried out by P.G.-F., P.A.-P., J.I., and J.J. EMPAD electronics and design was done by M.W.T. and P.P. and supervised by S.M.G. All authors discussed the results and implications. K.X.N., J.J., R.R., L.W.M., and D.A.M. wrote the paper.

Cornell has licensed the EMPAD to the FEI division of Thermo Fisher Scientific for commercial production. The authors declare that they have no competing financial interests.

APPENDIX A: FOURIER CONVENTION

Fourier transform convention:

$$F(\vec{k}) = \frac{1}{2\pi} \int f(\vec{r}) \exp(-i\vec{k} \cdot \vec{r}) d\vec{r}, \quad (\text{A1})$$

$$f(\vec{r}) = \frac{1}{2\pi} \int F(\vec{k}) \exp(i\vec{k} \cdot \vec{r}) d\vec{k}. \quad (\text{A2})$$

When using this convention, we get these properties:

$$\mathcal{F}[A(\vec{r})B(\vec{r})] = \frac{1}{2\pi} A(\vec{k}) \otimes B(\vec{k}), \quad (\text{A3})$$

$$\mathcal{F}[A(\vec{r}) \otimes B(\vec{r})] = 2\pi A(\vec{k})B(\vec{k}), \quad (\text{A4})$$

$$\mathcal{F}\left[\frac{\partial^n}{\partial x_i^n} A(\vec{r})\right] = (ik_i)^n A(\vec{k}), \quad (\text{A5})$$

where \otimes represents the convolution operator.

APPENDIX B: MEASURING POLARITY AND TORQUE TRANSFER FROM PROBABILITY CURRENT IMAGES

Here, we derive the central relationship that connects the measured probability current flow of an electron beam with wave function $\Psi(\vec{r}, \vec{r}_p)$ centered about probe position \vec{r}_p to the torque transfer using the strong phase approximation. The starting point is the measurement of the COM image, $\langle \vec{p} \rangle$ formed by scanning the probe position \vec{r}_p and measuring the angular distribution of scattered electron beam at each probe position $|\Psi(\vec{k}, \vec{r}_p)|^2$, where \vec{k} and \vec{r} are the conjugate variables

in the back focal plane and image plane, respectively [45,51]. A COM image has each pixel value equal to the centroid of the associated diffraction pattern, where

$$\langle \vec{p}(\vec{r}_p) \rangle = \int \hbar \vec{k} |\Psi(\vec{k}, \vec{r}_p)|^2 d\vec{k}, \quad (\text{B1})$$

which follows from the definition of $\langle \vec{p} \rangle$ written out in a momentum basis [45,51].

Expanding $\langle \vec{p} \rangle = \langle \Psi | \hat{p} | \Psi \rangle$ in a position basis and using $\hat{p} = -i\hbar \vec{\nabla}$, we obtain

$$\langle \vec{p}(\vec{r}_p) \rangle = -\hbar i \int \Psi^*(\vec{r}, \vec{r}_p) \vec{\nabla} \Psi(\vec{r}, \vec{r}_p) d\vec{r}. \quad (\text{B2})$$

Considering that the momentum operator is a Hermitian (i.e., self-adjoint operator), then

$$\langle \vec{p}(\vec{r}_p) \rangle = \hbar i \int \Psi(\vec{r}, \vec{r}_p) \vec{\nabla} \Psi^*(\vec{r}, \vec{r}_p) d\vec{r}. \quad (\text{B3})$$

Adding together the two last equations, we arrive to the conclusion that $\langle \vec{p} \rangle$ differs from the expectation value of probability current flow $\langle \vec{j} \rangle$ by a factor of twice the mass of the electron m [45,51]:

$$\begin{aligned} \langle \vec{p}(\vec{r}_p) \rangle &= \frac{\hbar}{2i} \int \Psi^*(\vec{r}, \vec{r}_p) \vec{\nabla} \Psi(\vec{r}, \vec{r}_p) \\ &\quad - \Psi(\vec{r}, \vec{r}_p) \vec{\nabla} \Psi^*(\vec{r}, \vec{r}_p) d\vec{r} = 2m \langle \vec{j} \rangle. \end{aligned} \quad (\text{B4})$$

From Eq. (B4), we find that the expectation value of momentum or COM $\langle \vec{p} \rangle$ can be used interchangeably with the probability current flow $\langle \vec{j} \rangle$. Furthermore, this is the classical definition of a current, where the rate of flow from an electric charge is related to the net flow of electron beam in the sample measured as $\langle \vec{p} \rangle$.

In Appendix B 1, we review the already derived connection between the COM images and the gradient of the potential to establish a consistent notation. In Appendix B 2, we derive the relationship between torque transfer and the COM images. In Appendixes B 3 and B 4, we show how polarity is encoded in the probability current flow to a pair of conjugate diffracted beams.

1. Relation between COM and potential gradient images

To connect $\langle \vec{p} \rangle$ of the exit wave to the scattering potential, we next make the strong phase approximation which should hold if the probe amplitude does not change dramatically in the sample. In the strong phase approximation, the exit wave function is just a product of the initial wave function Ψ_0 and a phase term from the sample potential $V(\vec{r})$:

$$\Psi(\vec{r}, \vec{r}_p) = \exp[i\sigma V(\vec{r})] \Psi_0(\vec{r} - \vec{r}_p), \quad (\text{B5})$$

where σ is the usual interaction parameter [42]. Substituting Eq. (B5) into Eq. (B2) gives

$$\begin{aligned} \langle \vec{p}(\vec{r}_p) \rangle &= -i\hbar \int [i\sigma \vec{\nabla} V(\vec{r}) \Psi_0(\vec{r} - \vec{r}_p) + \vec{\nabla} \Psi_0(\vec{r} - \vec{r}_p)] \\ &\quad \times \exp[i\sigma V(\vec{r})] \exp[-i\sigma V(\vec{r})] \Psi_0^*(\vec{r} - \vec{r}_p) d\vec{r}, \\ \langle \vec{p}(\vec{r}_p) \rangle &= -i\hbar \int \Psi_0^*(\vec{r} - \vec{r}_p) \vec{\nabla} \Psi_0(\vec{r} - \vec{r}_p) d\vec{r} \\ &\quad + \hbar\sigma \int \vec{\nabla} V(\vec{r}) |\Psi_0(\vec{r} - \vec{r}_p)|^2 d\vec{r}. \end{aligned} \quad (\text{B6})$$

If the beam is symmetric [52], then the first term goes to zero, and the second term can be written as a convolution:

$$\langle \vec{p}(\vec{r}_p) \rangle = \hbar\sigma |\Psi_0(\vec{r}_p)|^2 \otimes \vec{\nabla} V(\vec{r}_p), \quad (\text{B7})$$

which establishes the conditions under which the COM image is a convolution of the potential gradient and the probe. If the beam is not symmetric, then the first term, which depends only on the incident beam, provides a constant offset uniform background which can be subtracted off, and the second term changes Eq. (B7) to a cross-correlation [43].

2. Calculating torque from COM images

To calculate torque, we start with a relation in Ehrenfest's theorem that connects $\langle \vec{p} \rangle$ to the gradient of the projected potential [45,51]. Second, we find that the torque operator for an electron in the beam can be defined as

$$\hat{\Gamma} = \hat{r} \times -\vec{\nabla} \hat{V}. \quad (\text{B8})$$

We can calculate its expectation value by expanding in the position basis:

$$\langle \hat{\Gamma} \rangle = \langle \Psi | \hat{\Gamma} | \Psi \rangle, \quad (\text{B9})$$

and the z component is

$$\begin{aligned} \langle \hat{\Gamma}_z \rangle &= \int \langle \Psi | \vec{r}'' \rangle \langle \vec{r}'' | \hat{x} | \vec{r}' \rangle \langle \vec{r}' | -\frac{\partial \hat{V}}{\partial y} | \vec{r} \rangle \langle \vec{r} | \Psi \rangle d\vec{r} d\vec{r}' d\vec{r}'' \\ &\quad + \int \langle \Psi | \vec{r}'' \rangle \langle \vec{r}'' | \hat{y} | \vec{r}' \rangle \langle \vec{r}' | \frac{\partial \hat{V}}{\partial x} | \vec{r} \rangle \langle \vec{r} | \Psi \rangle d\vec{r} d\vec{r}' d\vec{r}'' . \end{aligned} \quad (\text{B10})$$

Since the position bases are eigenvectors of the position and potential operators, we can expand the integral:

$$\begin{aligned} \langle \hat{\Gamma}_z \rangle &= \int x \frac{-\partial V}{\partial y}(\vec{r}') \Psi^*(\vec{r}'') \Psi(\vec{r}) \delta(\vec{r}'' - \vec{r}') \delta(\vec{r}' - \vec{r}) \\ &\quad \times d\vec{r} d\vec{r}' d\vec{r}'' + \int y \frac{\partial V}{\partial x}(\vec{r}') \Psi^*(\vec{r}'') \Psi(\vec{r}) \delta(\vec{r}'' - \vec{r}') \\ &\quad \times \delta(\vec{r}' - \vec{r}) d\vec{r} d\vec{r}' d\vec{r}'' . \end{aligned} \quad (\text{B11})$$

We only show the calculation for one of the terms in the sum. Both are similar, and combining gives

$$\langle \hat{\Gamma}_z \rangle = \int x \frac{-\partial V}{\partial y} |\Psi(\vec{r})|^2 d\vec{r} + \int y \frac{\partial V}{\partial x} |\Psi(\vec{r})|^2 d\vec{r}. \quad (\text{B12})$$

This is the general formula where $\Psi(\vec{r})$ is the exit wave function. In the context of a scanning beam, we can write our exit wave function as the probe shifted to the relevant scan point $\Psi(\vec{r} - \vec{r}_p)$. We also want to measure with respect to \vec{r}_p as the origin. Therefore, we rewrite for the torque in the z direction as

$$\Gamma_z(\vec{r}_p) = \int \{(\vec{r} - \vec{r}_p) \times [-\vec{\nabla} V(\vec{r})]\}_z |\Psi(\vec{r} - \vec{r}_p)|^2 d\vec{r}, \quad (\text{B13})$$

where $V(\vec{r})$ is the potential of the specimen.

We take advantage of the symmetry of the probe to rewrite this equation to look like a convolution (for asymmetric

probes, this will remain a cross-correlation, a result which will carry through without loss of generality):

$$\Gamma_z(\vec{r}_p) = \int [(\vec{r}_p - \vec{r}) \times -\vec{\nabla}V(\vec{r})]_z |\Psi(\vec{r}_p - \vec{r})|^2 d\vec{r}. \quad (\text{B14})$$

Here, we have introduced Eqs. (B13) and (B14) in vector form, from which we could relate this back to Eq. (B12). Furthermore, convolutions in real space are multiplications in Fourier space [Eq. (A3)] which, by taking a Fourier transform, gives

$$\begin{aligned} \mathcal{F}[\Gamma_z(\vec{r})] &= -\mathcal{F}\left[\frac{-\partial V}{\partial y}(\vec{r})\right] \mathcal{F}[x|\Psi(\vec{r})|^2] + \mathcal{F}\left[\frac{\partial V}{\partial x}(\vec{r})\right] \\ &\quad \times \mathcal{F}[y|\Psi(\vec{r})|^2]. \end{aligned} \quad (\text{B15})$$

$$\Gamma_z(\vec{r}) = \mathcal{F}^{-1}\left\{\frac{-\mathcal{F}[\langle p_y(\vec{r}) \rangle] \mathcal{F}[x|\Psi(\vec{r})|^2] + \mathcal{F}[\langle p_x(\vec{r}) \rangle] \mathcal{F}[y|\Psi(\vec{r})|^2]}{\hbar\sigma \mathcal{F}[|\Psi(\vec{r})|^2]}\right\}. \quad (\text{B18})$$

This is the desired result, describing the torque in terms of only the experimentally measured quantities $\langle p_x(\vec{r}_p) \rangle$, $\langle p_y(\vec{r}_p) \rangle$, $|\Psi_0(\vec{r})|^2$. A key observation here is that, in the strong phase approximation [Eq. (B4)], $|\Psi(\vec{r})|^2 = |\Psi_0(\vec{r})|^2$, and the incident beam shape can be measured directly at medium resolution or with the aberration-correction software at high resolution. At medium spatial resolution (nonoverlapping disks), multislice simulations indicate this approximation is robust for sample thicknesses up to 20 nm at 300 keV.

Now $\mathcal{F}[|\Psi(\vec{r})|^2]$ is peaked at zero frequency and is zero at frequencies with k -vector magnitudes larger than the diameter of the probe-forming aperture. To avoid dividing by zero or by values arbitrarily close to zero in $\mathcal{F}[|\Psi(\vec{r})|^2]$, we pass this through a low-pass filter to suppress the high-frequency noise beyond the aperture cutoff. Equation (B18) can be trivially modified to incorporate an optimal Wiener filter, recognizing that Eq. (B18) is essentially deconvolving the effect of the probe contrast transfer function (CTF) from the torque mea-

At this point, we need to find the gradient of the potential. As shown in Eq. (B7), by using the strong phase approximation, our COM images are related to the gradient of the potential by a convolution. For example, the COM in the x direction is with Ψ_0 being the incident wave function given by

$$\langle p_x(\vec{r}_p) \rangle = \hbar\sigma |\Psi_0(\vec{r}_p)|^2 \otimes \frac{\partial V(\vec{r}_p)}{\partial x}. \quad (\text{B16})$$

Taking a Fourier transform gives

$$\mathcal{F}[\langle p_x(\vec{r}_p) \rangle] = \hbar\sigma \mathcal{F}[|\Psi(\vec{r})|^2] \mathcal{F}\left[\frac{\partial V}{\partial x}(\vec{r})\right]. \quad (\text{B17})$$

We can now write Eq. (B15) as

surement. Omitting the division by the probe CTF leaves us with the torque measurement blurred out to probe resolution. This may be preferable for noisy data or thick samples where the strong phase approximation may no longer hold.

3. Measuring polarity from the COM image in the strong phase approximation

Polarity is usually calculated within a Bloch-wave formalism [50] to account for the multiple scattering of the electron beam through the sample. While there are analytic results for special cases, that approach is more useful computationally than for insight. Here, we consider a thin sample described by the strong phase approximation that provides a simpler result, useful for understanding the contributions to the polarity measurement, while still retaining the key symmetries of the more complicated theory.

Starting with Eq. (B4), and as shown by Deb *et al.* [53], the diffraction pattern expanded out to third order is

$$\begin{aligned} |\Psi(\vec{k}, \vec{r}_p)|^2 &= |\Psi_0(\vec{k})|^2 + \frac{\sigma}{\pi} \text{Im}\{\Psi_0(\vec{k}, \vec{r}_p)[\Psi_0^*(\vec{k}, \vec{r}_p) \otimes V^*(\vec{k})]\} + \frac{\sigma^2}{4\pi^2} (|\Psi_0(\vec{k}, \vec{r}_p) \otimes V(\vec{k})|^2 \\ &\quad - \text{Re}\{\Psi_0(\vec{k}, \vec{r}_p)[\Psi_0^*(\vec{k}, \vec{r}_p) \otimes V_2^*(\vec{k})]\}) + \frac{\sigma^3}{8\pi^3} (\text{Im}\{[\Psi_0(\vec{k}, \vec{r}_p) \otimes V(\vec{k})][\Psi_0^*(\vec{k}, \vec{r}_p) \otimes V_2^*(\vec{k})]\}) \\ &\quad - \frac{1}{3} \text{Im}\{\Psi_0(\vec{k}, \vec{r}_p)[\Psi_0^*(\vec{k}, \vec{r}_p) \otimes V_3^*(\vec{k})]\}) + \dots, \end{aligned} \quad (\text{B19})$$

where

$$\Psi_0(\vec{k}, \vec{r}_p) = \Psi_0(\vec{k}) \exp(-i\vec{k} \cdot \vec{r}_p), \quad (\text{B20})$$

$$V_2(\vec{k}) = V(\vec{k}) \otimes V(\vec{k}), \quad (\text{B21})$$

$$V_3(\vec{k}) = V(\vec{k}) \otimes V(\vec{k}) \otimes V(\vec{k}). \quad (\text{B22})$$

The only term outside the bright disk field that is asymmetric and therefore contributes to the COM signal from the diffracted beams is the third-order term:

$$\text{Im}\{[\Psi_0(\vec{k}, \vec{r}_p) \otimes V(\vec{k})][\Psi_0^*(\vec{k}, \vec{r}_p) \otimes V_2^*(\vec{k})]\}. \quad (\text{B23})$$

We assume our sample is a crystal and can therefore write our crystal potential in reciprocal space as

$$V(\vec{k}) = \mathcal{F}[V(\vec{r})] = \sum_{\vec{G}} U_{\vec{G}} \exp(i\phi_{\vec{G}}) \delta(\vec{k} - \vec{G}), \quad (\text{B24})$$

where $\vec{G} = h\vec{g}_1 + k\vec{g}_2 + l\vec{g}_3$ is a reciprocal lattice vector and $U_{\vec{G}}$ and $\phi_{\vec{G}}$ are real. Substituting $V(\vec{k})$ from Eq. (B24) into Eq. (B23) introduces three sums over reciprocal lattice vectors labeled $\vec{G}_1, \vec{G}_2, \vec{G}_3$, and after some algebra, Eq. (B23) becomes

$$\begin{aligned} & \text{Im}\{[\Psi_0(\vec{k}, \vec{r}_p) \otimes V(\vec{k})][\Psi_0^*(\vec{k}, \vec{r}_p) \otimes V_2^*(\vec{k})]\} \\ &= \sum_{\vec{G}_1, \vec{G}_2, \vec{G}_3} \Psi_0(\vec{k} - \vec{G}_1) \Psi_0^*(\vec{k} - \vec{G}_2 - \vec{G}_3) U_{\vec{G}_1} U_{\vec{G}_2} U_{\vec{G}_3} \\ & \times \sin(\phi_{\vec{G}_1} - \phi_{\vec{G}_2} - \phi_{\vec{G}_3}). \end{aligned} \quad (\text{B25})$$

$$\begin{aligned} & \int \vec{k} \sum_{\vec{G}_2} |\Psi_0(\vec{k} - \vec{G}_1)|^2 U_{\vec{G}_1} U_{\vec{G}_2} U_{\vec{G}_1 - \vec{G}_2} \sin(\phi_{\vec{G}_1} - \phi_{\vec{G}_2} - \phi_{\vec{G}_1 - \vec{G}_2}) d\vec{k} + \int \vec{k} \sum_{\vec{G}_3} |\Psi_0(\vec{k} + \vec{G}_1)|^2 U_{-\vec{G}_1} U_{\vec{G}_3} U_{\vec{G}_1 - \vec{G}_3} \\ & \times \sin(\phi_{-\vec{G}_1} - \phi_{\vec{G}_3} - \phi_{\vec{G}_1 - \vec{G}_3}) d\vec{k}, \end{aligned} \quad (\text{B26})$$

where we have separated the integral for later convenience. We can make a variable substitution for the integration variables \vec{k} so that they are centered around the diffraction spot:

$$\begin{aligned} & \sum_{\vec{G}_2} U_{\vec{G}_1} U_{\vec{G}_2} U_{\vec{G}_1 - \vec{G}_2} \sin(\phi_{\vec{G}_1} - \phi_{\vec{G}_2} - \phi_{\vec{G}_1 - \vec{G}_2}) \int (\vec{k} + \vec{G}_1) |\Psi_0(\vec{k})|^2 d\vec{k} + \sum_{\vec{G}_3} U_{-\vec{G}_1} U_{\vec{G}_3} U_{\vec{G}_1 - \vec{G}_3} \\ & \times \sin(\phi_{-\vec{G}_1} - \phi_{\vec{G}_3} - \phi_{\vec{G}_1 - \vec{G}_3}) \int (\vec{k} - \vec{G}_1) |\Psi_0(\vec{k})|^2 d\vec{k} \end{aligned} \quad (\text{B27})$$

The first part of each integral $\int \vec{k} |\Psi_0(\vec{k})|^2 d\vec{k}$ is just the first moment of the unscattered bright-field disk, which is zero for a nonaberrated or symmetric incident beam. The second part is just the total intensity of the beam I_0 times the reciprocal lattice vector. This simplifies the expression to

$$\vec{G}_1 I_0 \sum_{\vec{G}_2} U_{\vec{G}_1} U_{\vec{G}_2} U_{\vec{G}_1 - \vec{G}_2} \sin(\phi_{\vec{G}_1} - \phi_{\vec{G}_2} - \phi_{\vec{G}_1 - \vec{G}_2}) - \vec{G}_1 I_0 \sum_{\vec{G}_3} U_{-\vec{G}_1} U_{\vec{G}_3} U_{\vec{G}_1 - \vec{G}_3} \sin(\phi_{-\vec{G}_1} - \phi_{\vec{G}_3} - \phi_{\vec{G}_1 - \vec{G}_3}). \quad (\text{B28})$$

We can re-index $\vec{G}_3 = -\vec{G}_2$ without changing the second summation:

$$\vec{G}_1 I_0 \sum_{\vec{G}_2} U_{\vec{G}_1} U_{\vec{G}_2} U_{\vec{G}_1 - \vec{G}_2} \sin(\phi_{\vec{G}_1} - \phi_{\vec{G}_2} - \phi_{\vec{G}_1 - \vec{G}_2}) - U_{-\vec{G}_1} U_{-\vec{G}_2} U_{-\vec{G}_1 + \vec{G}_2} \sin(\phi_{-\vec{G}_1} - \phi_{-\vec{G}_2} - \phi_{-\vec{G}_1 + \vec{G}_2}). \quad (\text{B29})$$

For a real potential $V(\vec{r})$, $V^*(\vec{k}) = V(-\vec{k})$. This means $U_{\vec{G}} = U_{-\vec{G}}$ and $\phi_{\vec{G}} = -\phi_{-\vec{G}}$, which gives our final expression for the COM of the Friedel pair:

$$\langle \vec{p}_{\{\vec{G}_1\}} \rangle = \left(\frac{\hbar\sigma^3}{8\pi^3} \right) 2\vec{G}_1 I_0 \sum_{\vec{G}_2} U_{\vec{G}_1} U_{\vec{G}_2} U_{\vec{G}_1 - \vec{G}_2} \sin(\phi), \quad (\text{B30})$$

where three-phase invariant $\phi = \phi_{\vec{G}_1} - \phi_{\vec{G}_2} - \phi_{\vec{G}_1 - \vec{G}_2}$ as before. However, if the crystal is also centrosymmetric, i.e., $V(\vec{r}) = V(-\vec{r})$, then the Fourier transform is also pure real, so

Equation (B25) gives rise to the polarity term, and the phase portion in Eq. (B25) is recognized as the three-phase invariant of crystallography:

$$\phi = \phi_{\vec{G}_1} - \phi_{\vec{G}_2} - \phi_{\vec{G}_1 - \vec{G}_2}, \quad (\text{B26})$$

which is invariant under a change of origin in real space: A shift in the origin by \vec{r}_0 leads to a phase shift $\phi'_{\vec{G}} = \phi_{\vec{G}} + \vec{G} \cdot \vec{r}_0$, but as the vectors $\vec{G}_1 - \vec{G}_2 - \vec{G}_1 + \vec{G}_2 = 0$, the offset $(\vec{G}_1 - \vec{G}_2 - \vec{G}_1 + \vec{G}_2) \cdot \vec{r}_0 = 0$ as well; thus, there is no phase shift when choosing a new origin, making $\sin(\phi)$ a good metric for tracking components of the polar order parameter.

4. Polarity from the COM of conjugate diffraction spots

Polarity can be sensed most simply using Friedel pairs at \vec{G}_1 and $-\vec{G}_1$. Focusing on the diffraction spot centered around \vec{G}_1 , we remove the \vec{G}_1 summation from Eq. (B25) and similarly for $-\vec{G}_1$. The probability current flow given by the COM measurement will then become the sum of the first moments of the \vec{G}_1 and $-\vec{G}_1$ spots:

all $\phi_{\vec{G}} = 0$ which means Eq. (B30) simplifies to 0 for nonpolar materials. This result remains 0 even under a shift in origin that breaks the even symmetry of the crystal potential $V(\vec{r})$ thanks to the three-phase invariant. More generally, as $\sin(\phi)$ is independent of the choice of origin in real space, it can be used as a good order parameter for describing the component of the polarity along \vec{G}_1 .

Finally, the Fourier coefficients of the potential $U_{\vec{G}}$ are sensitive to both the nuclear and electronic contributions of the total potential for electron scattering. In other words, the measured dipole density probed is net/total dipole density.

- [1] N. Choudhury, L. Walizer, S. Lisenkov, and L. Bellaiche, *Nature (London)* **470**, 513 (2011).
- [2] A. K. Yadav, C. T. Nelson, S. L. Hsu, Z. Hong, J. D. Clarkson, C. M. Schlepütz, A. R. Damodaran, P. Schafer, E. Arenholz, L. Dedon *et al.*, *Nature (London)* **530**, 198 (2016).
- [3] L. W. Martin and A. M. Rappe, *Nat. Rev. Mater.* **2**, 16087 (2016).
- [4] Y. Nahas, S. Prokhorenko, L. Louis, Z. Gui, I. Kornev, and L. Bellaiche, *Nat. Commun.* **6**, 8542 (2015).
- [5] J. Hong, G. Catalan, D. N. Fang, E. Artacho, and J. F. Scott, *Phys. Rev. B* **81**, 172101 (2010).
- [6] S. Prosandeev, I. Ponomareva, I. Naumov, I. Kornev, and L. Bellaiche, *J. Phys.: Condens. Matter* **20**, 193201 (2008).
- [7] H. Schmid, *J. Phys.: Condens. Matter* **20**, 434201 (2008).
- [8] I. I. Naumov, L. Bellaiche, and H. Fu, *Nature (London)* **432**, 737 (2004).
- [9] L. Baudry, A. Sené, I. A. Luk'yanchuk, L. Lahoche, and J. F. Scott, *Phys. Rev. B* **90**, 024102 (2014).
- [10] W. J. Chen, Y. Zheng, and B. Wang, *Sci. Rep.* **5**, 11165 (2015).
- [11] Y. Tikhonov, S. Kondovych, J. Mangeri, M. Pavlenko, L. Baudry, A. Sene, A. Galda, S. Nakhmanson, O. Heinonen, A. Razumnaya *et al.*, *Sci. Rep.* **10**, 8657 (2020).
- [12] S. Yuan, W. J. Chen, L. L. Ma, J. Ye, W. M. Xiong, J. Y. Liu, Y. L. Liu, B. Wang, and Y. Zheng, *Acta Mater.* **148**, 330 (2018).
- [13] W. J. Chen, S. Yuan, L. L. Ma, J. Ye, B. Wang, and Y. Zheng, *RSC Adv.* **8**, 4434 (2018).
- [14] Y. L. Tang, Y. L. Zhu, X. L. Ma, A. Y. Borisevich, A. N. Morozovska, E. A. Eliseev, W. Y. Wang, Y. J. Wang, Y. B. Xu, Z. D. Zhang *et al.*, *Science* **348**, 547 (2015).
- [15] S. Das, Y. L. Tang, Z. Hong, M. A. P. Goncalves, M. R. McCarter, C. Klewe, K. X. Nguyen, F. Gomez-Ortiz, P. Schafer, E. Arenholz *et al.*, *Nature (London)* **568**, 368 (2019).
- [16] Y. J. Wang, Y. P. Feng, Y. L. Zhu, Y. L. Tang, L. X. Yang, M. J. Zou, W. R. Geng, M. J. Han, X. W. Guo, B. Wu *et al.*, *Nat. Mater.* **19**, 881 (2020).
- [17] L. Berger, *Phys. Rev. B* **54**, 9353 (1996).
- [18] E. B. Myers, D. C. Ralph, J. A. Katine, R. N. Louie, and R. A. Buhrman, *Science* **285**, 867 (1999).
- [19] J. C. Slonczewski, *J. Magn. Magn. Mater.* **159**, L1 (1996).
- [20] M. Tsoi, A. G. M. Jansen, J. Bass, W. C. Chiang, M. Seck, V. Tsoi, and P. Wyder, *Phys. Rev. Lett.* **80**, 4281 (1998).
- [21] P. Shafer, P. Garcia-Fernandez, P. Aguado-Puente, A. R. Damodaran, A. K. Yadav, C. T. Nelson, S. L. Hsu, J. C. Wojdel, J. Iniguez, L. W. Martin *et al.*, *Proc. Natl. Acad. Sci. USA* **115**, 915 (2018).
- [22] I. MacLaren, L. Q. Wang, D. McGrouther, A. J. Craven, S. McVitie, R. Schierholz, A. Kovacs, J. Barthel, and R. E. Dunin-Borkowski, *Ultramicroscopy* **154**, 57 (2015).
- [23] Y. Han, K. Nguyen, M. Cao, P. Cueva, S. Xie, M. W. Tate, P. Purohit, S. M. Gruner, J. Park, and D. A. Muller, *Nano Lett.* **18**, 3746 (2018).
- [24] K. X. Nguyen, Y. Jiang, M. C. Cao, P. Purohit, A. K. Yadav, P. Garcia-Fernandez, M. W. Tate, C. S. Chang, P. Aguado-Puente, J. Iniguez *et al.*, [arXiv:2012.04134](https://arxiv.org/abs/2012.04134).
- [25] P. Behera, M. A. May, F. Gomez-Ortiz, S. Susarla, S. Das, C. T. Nelson, L. Caretta, S. L. Hsu, M. R. McCarter, B. H. Savitzky *et al.*, *Sci. Adv.* **8**, eabj8030 (2022).
- [26] A. K. Yadav, K. X. Nguyen, Z. Hong, P. Garcia-Fernandez, P. Aguado-Puente, C. T. Nelson, S. Das, B. Prasad, D. Kwon, S. Cheema *et al.*, *Nature (London)* **565**, 468 (2019).
- [27] A. R. Damodaran, J. D. Clarkson, Z. Hong, H. Liu, A. K. Yadav, C. T. Nelson, S. L. Hsu, M. R. McCarter, K. D. Park, V. Kravtsov *et al.*, *Nat. Mater.* **16**, 1003 (2017).
- [28] J. C. Wojdel, P. Hermet, M. P. Ljungberg, P. Ghosez, and J. Iniguez, *J. Phys.: Condens. Matter* **25**, 305401 (2013).
- [29] V. Grillo, G. C. Gazzadi, E. Karimi, E. Mafakheri, R. W. Boyd, and S. Frabboni, *Appl. Phys. Lett.* **104**, 043109 (2014).
- [30] B. J. McMorrán, A. Agrawal, I. M. Anderson, A. A. Herzing, H. J. Lezec, J. J. McClelland, and J. Unguris, *Science* **331**, 192 (2011).
- [31] J. Verbeeck, H. Tian, and P. Schattschneider, *Nature (London)* **467**, 301 (2010).
- [32] M. Uchida and A. Tonomura, *Nature (London)* **464**, 737 (2010).
- [33] A. H. Tavabi, P. Rosi, E. Rotunno, A. Roncaglia, L. Belsito, S. Frabboni, G. Pozzi, G. C. Gazzadi, P. H. Lu, R. Nijland *et al.*, *Phys. Rev. Lett.* **126**, 094802 (2021).
- [34] T. Schachinger, S. Löffler, A. Steiger-Thirsfeld, M. Stöger-Pollach, S. Schneider, D. Pohl, B. Rellinghaus, and P. Schattschneider, *Ultramicroscopy* **179**, 15 (2017).
- [35] M. W. Tate, P. Purohit, D. Chamberlain, K. X. Nguyen, R. Hovden, C. S. Chang, P. Deb, E. Turgut, J. T. Heron, D. G. Schlom *et al.*, *Microsc. Microanal.* **22**, 237 (2016).
- [36] C. Kittel, *Introduction to Solid State Physics*, 8th ed. (John Wiley & Sons, Singapore, 2005).
- [37] R. D. King-Smith and D. Vanderbilt, *Phys. Rev. B* **47**, 1651 (1993).
- [38] A. Lubk, A. Beche, and J. Verbeeck, *Phys. Rev. Lett.* **115**, 176101 (2015).
- [39] M. J. Humphry, B. Kraus, A. C. Hurst, A. M. Maiden, and J. M. Rodenburg, *Nat. Commun.* **3**, 730 (2012).
- [40] J. M. Rodenburg and R. H. T. Bates, *Philos. Trans. A Math. Phys. Eng. Sci.* **339**, 521 (1992).
- [41] Y. Jiang, Z. Chen, Y. Han, P. Deb, H. Gao, S. Xie, P. Purohit, M. W. Tate, J. Park, S. M. Gruner *et al.*, *Nature (London)* **559**, 343 (2018).
- [42] E. J. Kirkland, *Advanced Computing in Electron Microscopy* (Springer, Cham, 2020).
- [43] I. Lazic, E. G. T. Bosch, and S. Lazar, *Ultramicroscopy* **160**, 265 (2016).
- [44] N. H. Dekkers and H. D. Lang, *Optik* **41**, 452 (1974).
- [45] A. Lubk and J. Zweck, *Phys. Rev. A* **91**, 023805 (2015).
- [46] J. N. Chapman, P. E. Batson, E. M. Waddell, and R. P. Ferrier, *Ultramicroscopy* **3**, 203 (1978).
- [47] E. M. Waddell and J. N. Chapman, *Optik* **54**, 83 (1979).
- [48] J. D. Jackson, *Classical Electrodynamics*, 3rd ed. (Wiley, New York, 1999).
- [49] C. Kittel, *Phys. Rev.* **70**, 965 (1946).
- [50] J. M. Zuo and J. C. H. Spence, *Electron Microdiffraction*, 1st ed. (Springer US, New York, 1993).
- [51] K. Müller, F. F. Krause, A. Béché, M. Schowalter, V. Galioit, S. Löffler, J. Verbeeck, J. Zweck, P. Schattschneider, and A. Rosenauer, *Nat. Commun.* **5**, 5653 (2014).
- [52] M. C. Cao, Y. Han, Z. Chen, Y. Jiang, K. X. Nguyen, E. Turgut, G. D. Fuchs, and D. A. Muller, *Microscopy* **67**, i150 (2018).
- [53] P. Deb, M. C. Cao, Y. Han, M. E. Holtz, S. Xie, J. Park, R. Hovden, and D. A. Muller, *Ultramicroscopy* **215**, 113019 (2020).